RSC Advances

RSC Publishing

PAPER

View Article Online
View Journal | View Issue

Cite this: *RSC Advances*, 2013, **3**, 8504

Mg_3Sb_2-based Zintl compound: a non-toxic, inexpensive and abundant thermoelectric material for power generation†

A. Bhardwaj, A. Rajput, A. K. Shukla, J. J. Pulikkotil, A. K. Srivastava, A. Dhar, Govind Gupta, S. Auluck, D. K. Misra* and R. C. Budhani

The deployment of thermoelectric materials for deriving an enhanced figure of merit (*ZT*) for power generation in inexpensive, non-toxic and relatively abundant bulk homogeneous solid relies on the extent of achieving the ''phonon-glass electron crystal'' (PGEC) characteristics. Here, a proof of principal has been established experimentally in the present work for a Zintl compound of Mg_3Sb_2 and its derivative of isoelectronically Bi doped Bi; $Mg_3Sb_{2-x}Bi_x$ ($0 \leqslant x \leqslant 0.4$) alloys in Mg_3Sb_2. Single phase p-type Mg_3Sb_2 compounds, with Mg and Sb powders as starting materials, have been prepared directly by spark plasma sintering (SPS) in a one step process. The structural refinements of this hexagonal Zintl compound by X-ray diffraction analysis (XRD) and high resolution transmission electron microscopy (HRTEM) investigation reveal that they are single phase devoid of any oxides or Sb precipitates. Transport measurements indicate low thermoelectric figure of merit (*ZT* = 0.26 at 750 K) for Mg_3Sb_2. However, an optimum doping of 0.2 at% with iso-electronic Bi ions at the Sb site enhances the *ZT* to 0.6 at 750 K, which is comparable with the present day industrial materials such as Bi based tellurides and selenides which are toxic. We note that the system becomes metal with carrier density exceeding $15 \times 10^{20}/cm^3$ for $x \geqslant 0.25$. The substantial increase in *ZT* in $Mg_3Sb_{2-x}Bi_x$ ($0 \leqslant x \leqslant 0.4$) owes to a partial decoupling of the electronic and phonon subsystem, as expected for a Zintl phase compound. While the reduction in thermal conductivity in $Mg_3Sb_{2-x}Bi_x$ ($0 \leqslant x \leqslant 0.4$) accounts to mass fluctuations and grain boundary scattering, the enhancement in the electronic power-factor is attributed to the presence of heavy and light bands in its valence band structure. The latter has been confirmed by means of both X-ray photo electron spectroscopy studies and first-principles density functional based calculations. These measurements established that a high figure of merit can be achieved in this class of materials with appropriate doping. Further, relative abundance of the material ingredients combined with its one step synthesis leads to a cost effective production and less toxicity makes the material an environmentally benign system for thermoelectric power generation.

Received 25th January 2013,
Accepted 20th March 2013

DOI: 10.1039/c3ra40457a

www.rsc.org/advances

I. Introduction

The design of thermoelectric materials for deriving an enhanced figure of merit in a bulk homogeneous solid relies on the extent of achieving the ''phonon-glass electron crystal'' (PGEC)[1] characteristics. A complete manifestation of PGEC in a thermoelectric material is less practical as it suggests a decoupling of the electronic and phonon degrees of freedom of the crystal. In the recent past the Zintl phase compounds, which have a unique chemical bonding,[2–10] have been found to partly satisfy the PGEC criteria. These compounds are composed of highly electropositive cations (typically, related to group 1 and 2) that donate their electrons to electronegative anions; which, in turn, are used to form bonds in order to satisfy valency. The extent of charge transfer by the cations to the anion network establishes the ''electron crystal'' features for improving electronic transport, while the electropositive ions which act as phonon scattering centers, stands to its ''phonon glass'' behavior leading to a reduction in the thermal conductivity. As a result, a high thermoelectric figure of merit (*ZT*) has been attained in a variety of Zintl compounds such as skutterudites,[11–16] calthrates,[17–25] and others.[2,26–48] However, the composition of such materials generally has expensive rare-earth elements and toxic chalcogenides as constituents, together with the complex synthesis routes that make them less useful for large scale waste heat recovery applications.

Other than the Zintl phase compound, remarkable progress on state-of-art materials such as bismuth telluride based,[49–52] III-nitride based *e.g.* AlInN, InGaN[53–57] and silicon germanium

CSIR-Network of Institutes for Solar Energy, Materials Physics & Engineering Division, CSIR-National Physical Laboratory, Dr K. S. Krishnan Road, New Delhi, 110012, India. E-mail: misradk@nplindia.org; dakkmisra@gmail.com

† Electronic supplementary information (ESI) available. See DOI: 10.1039/c3ra40457a

alloys[58,59] has been made in the direction of exploring high performance thermoelectric materials. Several approaches such as defects, solid solution alloying, mass fluctuation, optimal doping and nano structuring in these materials were adopted to achieve high figure of merit (*ZT*) for efficient thermoelectric devices. Among several thermoelectric materials, Zintl phase compound namely Mg_3Sb_2 studied here exhibits a characteristic feature of PGEC that intrinsically enables to optimize the three competing parameters in the equation of thermoelectric figure of merit (*ZT*). The performance of TE materials is gauged by *ZT* which is defined as $ZT = S^2\sigma T/\kappa$ where S represents the Seebeck coefficient, σ the electrical conductivity and $\kappa_{el} + \kappa_{lattice}$ is the thermal conductivity accounting both the electrical (κ_{el}) and lattice ($\kappa_{lattice}$) contributions. Although the crystal structure and its bonding characteristics have been detailed by Zintl and Husemann,[60] limited efforts have been made towards the optimization of its thermoelectric figure of merit for high temperature applications.

II. Crystal structure and literature survey

Mg_3Sb_2 crystallizes both in cubic bixbyite as well as in hexagonal structures.[61] The cubic bixbyite structure (the α-phase) prototypical of La_2O_3 is the high temperature phase with 80 atoms unit cell (48 Mg and 32 Sb). Below ~1200 K, a structural phase transition to hexagonal phase (the β-phase) occurs with unit cell composed of 5 atoms (3 Mg and 2 Sb). The hexagonal structure is Mn_2O_3 type, (space group symmetry $P\bar{3}ml$, No. 164) with two inequivalent Mg sites, denoted as Mg(I) and Mg(II), occupying the 1b (0, 0, 0.5) and 2d (1/3, 2/3, 0.834) Wyckoff positions, respectively and the Sb atoms at 2d (1/3, 2/3, 0.228). The generated crystal structure of β-Mg_3Sb_2 for above mentioned crystallographic details is shown in Fig. 1.

Several groups[62–65] have reported difficulties in synthesizing the hexagonal Mg_3Sb_2 in its single phase and thus no significant progress has been made towards its viability for thermoelectric applications. Verbrugge *et al.*,[63] reported Mg–Sb alloys to be very similar to the known Pb–Te alloys with the advantage of having smaller mass density and lower vapor pressure. However, they observed a low $ZT \approx 0.1$ in the marginally stoichiometric Mg_3Sb_2 and proposed that dilute alloying would improve its thermoelectric properties. According to the reports of Kajikawa *et al.*,[64] the *ZT* of Mg_3Sb_2 was found to be ~0.55 at 600 K and this enhancement was attributed to the typical microstructural features induced by the hot pressing technique. However, a lack of microstructural details and analysis of crystallographic phases in their reports makes this class of materials quite interesting for further studies. In a previous report,[65] microstructural characterization of Mg_3Sb_2, synthesized by different routes, has been carried out and a reasonably low value of $ZT \approx 0.2$ at 875 K was reported for this material, containing measurable oxygen content at grain boundaries. These inconsistencies in the transport properties and *ZT* values are therefore intimately linked to the synthesis and processing of the material, and the microstructural details.

Several unanswered questions of fundamental nature as perceived from the previous studies,[63–65] combined with the relatively high abundance of Mg, Sb and Bi for low cost thermoelectrics, coupled with their nontoxicity in comparison with other Zintl phases that involve rare-earths and chalcogenides, have prompted us to carry out a systematic study of

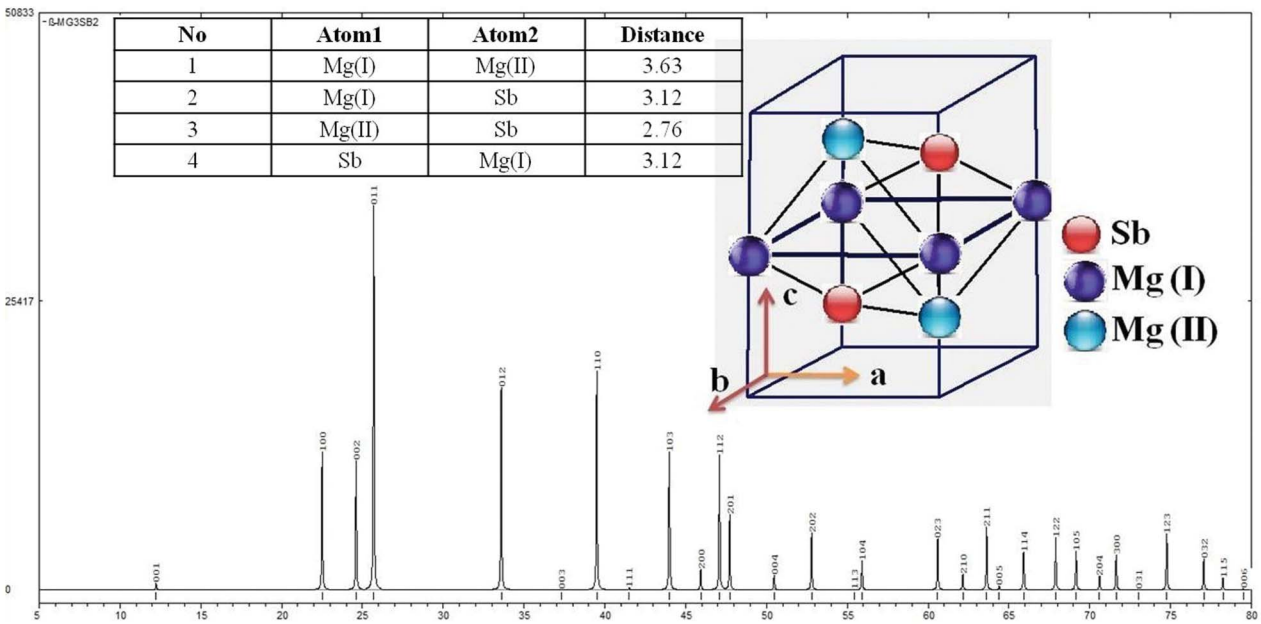

Fig. 1 The generated XRD spectrum and crystal structure for hexagonal β-Mg_3Sb_2 with atom bond length (inset).

the structure-property relationship of Mg_3Sb_2 alloys, namely that of $Mg_3Sb_{2-x}Bi_x$ in the composition range $0 \leqslant x \leqslant 0.4$. The salient features of our present work include (i) successful deployment of spark plasma sintering (SPS) technique as one step rapid-sintering synthesis process in crystallizing $Mg_3Sb_{2-x}Bi_x$ alloys devoid of oxygen impurities with relatively high density samples (ii) characterization of S (T), σ (T) and κ (T) for $300 \leqslant T \leqslant 750$ K, for providing an estimation of $(ZT)_{max}$ $\approx$0.60 at 750 K in $Mg_3Sb_{2-x}Bi_x$; x = 0.2, alloys, and (iii), electronic structure and chemical bonding characterization using X-ray photo-emission spectroscopy (XPS), supported by first-principles calculations based on density functional theory.

III. Methods

III.A. Materials processing and structure determination

High purity elements Mg, Sb and Bi (99.99%, Alfa Aesar) for synthesizing $Mg_3Sb_{2-x}Bi_x$ ($0 \leqslant x \leqslant 0.4$) were blended by mechanical milling and subsequently ground in an agate mortar. The blended powders were then subjected to spark plasma sintering (SPS) at a temperature and pressure of 1073 K and 50 MPa, respectively, for a holding time of 10 min. Pellets of 12.7 mm in diameter were obtained. The density of these samples was measured by using an Archimedes' kit and was observed 99% of the theoretical density.

The determination of crystallographic structure of $Mg_3Sb_{2-x}Bi_x$, samples was carried out by powder X-ray diffractometery (Rigaku Mini Flex II) in reflection θ–2θ geometry, with position sensitive detector (Ultafast D Tex), operating at 30 kV and 20 mA, using a graphite monochromator and Cu-Kα radiation with wavelength λ = 1.5406 Å along with $CuK_{\alpha 2}$ filter and rotating anode equipped with powder 2θ diffractometer ranging from 20 to 80 degrees. The experimental conditions and parameters such as sample size, power ratings of X-ray tube (30 kV, 20 mA) and other diffractometer parameters such as scan speed, counting steps *etc.* were kept constant for all diffraction experiments.

The microstructure investigation of the bulk samples of $Mg_3Sb_{2-x}Bi_x$ was carried out using a HRTEM (model: Technai G2 F30; STWIN) operating at 300 kV. The TEM specimens were prepared in three steps. Initially, the SPS processed pellets were cut into 3 mm discs using an ultrasonic disc cutter (model: Gaton 170). The specimen was then mechanically polished with a load of 12 g using a dimple grinder (model: South Bay Technology 515) and finally an electron transparent specimen for TEM analysis was achieved by Ar^+-ion milling (model: Boltech RES 101). The ion milling was carried out in two steps using a cold stage held at constant temperature of 160 K. The specimens were first milled to perforation over 2 h at 3.5 kV and 5 mA with a 6° milling angle followed by further milling for 30 min at 1 kV and 5 mA with a milling angle of 4°. The elemental analysis of the samples was performed using energy dispersive spectroscopy (EDS) attached to the TEM.

III.B. Thermoelectric transport

Thermal diffusivity of $Mg_3Sb_{2-x}Bi_x$ samples were measured on a laser flash system (Lineseis, LFA 1000) using disk-shaped specimens with approximate thickness of 2.5 mm and diameter of 12.7 mm. A graphite reference material was measured alongside each sample. Specific heat was determined by a DSC instrument (822^e Mettler Toledo). The thermal conductivity of the sample was calculated using the relation $\kappa = \alpha \times C_p \times \rho$, where α the thermal diffusivity, ρ the geometrical pellet density and C_p the heat capacity. For the measurement of S (T) and resistivity, rectangular bar specimens of $3.0 \times 2.5 \times 9$ mm^3 were cut from the pellets and used for four-probe electrical conductivity using a commercial equipment (ULVAC, ZEM3). The transport data was collected over the temperature range of 300 K to 773 K at the increments of 25 K, using ΔT values of 5, 10 and 15 K for all temperature steps. The processing and thermoelectric characterization of $Mg_3Sb_{2-x}Bi_x$ samples were repeated three times in order to confirm the reproducibility of our present data. It was found that the thermoelectric properties were reproducible within 3% under identical experimental conditions.

III.C. Electronic structure

III.C.1. X-Ray photo electron spectroscopy (XPS). XPS experiments were carried out in a multi-chamber ultra-high vacuum (UHV) surface science system where the base pressure was in the 10^{-10} mbar range. The chamber is equipped with an Omicron EA 125 electron energy analyzer and monochromated Al K_α X-ray source. All binding energies have been referenced to the Fermi edge of an Ar^+ sputtered clean polycrystalline Ag sample. The XPS data has been collected using 20 eV analyzer pass energy which results in an overall energy resolution of 0.37 eV determined from the Fermi edge broadening of polycrystalline Ag. Clean surfaces of the samples were obtained by *in situ* repeated mechanical scrapping using a diamond file and cleanliness of the prepared surfaces are evident from the absence of C and O 1s signals in the survey spectra (Fig. S2, ESI†). The composition of the samples have been determined from the normalized area under the curve of Mg 2s and Sb 4d core levels of Mg_3Sb_2 and Mg 2s, Sb 4d, and Bi 4f core levels for $Mg_3Sb_{1.8}Bi_{0.2}$. These spectra are recorded under similar conditions, *i.e.* comparable analyzer settings, X-ray source intensity and sample position. Area under the curve of each core level used in composition calculation was normalized by respective photoemission cross section, inelastic mean free path and analyzer transmission function.

III.C.2 First-principles calculations. The first principle calculations is an important finding to study the theoretical equilibrium structure in terms of internal coordinates of atoms, electronic structure, and optical properties. Several Zintl compounds have been studied by using first principle calculation to investigate the electronic and optical properties.[66–73] Here, we also studied the electronic structure of Mg_3Sb_2 by using density functional theory. In order to obtain the theoretical equilibrium structure in terms of internal coordinates, we performed LAPW calculations using the WIEN2k program package.[74,75] The lattice parameters were

fixed to the experimental values. The atomic positions were relaxed by using a dampened Newton scheme, based on the minimization of Hellmann–Feynman forces to values smaller than 5 meV $Å^{-1}$. Self-consistency was achieved when the variation in the total energies between two consecutive iterations was smaller than 10^{-5} eV. The charge density is converged to 10^{-4}. The basis sets was constructed with $R_{MT}K_{Max}$ = 8.0, G_{max} = 24 and l_{max} = 10. The LAPW sphere radii, R_{MT} for Mg and Sb were chosen to be 2.2 a_0, where a_0 is the Bohr radius. The Brillouin zone integration was performed with 360 k-points distributed over the irreducible wedge of the hexagonal Brillouin zone. The magnitude of the energy band gap is crucial and hence we have used the modified Becke–Johnson (mBJ) scheme to account for the exchange and correlation effects of the crystal. It is observed that the mBJ potential predicts the band gaps with higher precision in comparison to the experiments and is certainly better than the conventional parameterization based on the local density approximation (LDA) and generalized gradient approximation (GGA).

Self-consistent tight-binding (TB) calculations were also performed using the linear muffin-tin-orbital (LMTO) method in the atomic sphere approximation (ASA).[76] The choice of the Wigner–Seitz radii of the atomic constituents were assigned automatically resulting in a 16% overlap restriction and combined correction terms were included.[77] To satisfy the overlap criteria of the atomic spheres in the TB-LMTO-ASA method, three empty spheres at sites (0, 0, 0), (1/3, 2/3, 0.4137) and (1/2, 1/2, 1/2) were incorporated into the basis set. A basis set of Mg 3s/3p/(3d), and Sb 5s/5p/(5d)/(5f) were employed, with the down-folded orbitals representing that given in parentheses. The Brillouin zone integrations were performed on a grid of 24 × 24 × 16 resulting in 885 irreducible k-points. Scalar relativistic corrections were included in the crystal Hamiltonian. For bonding analysis, the energy contributions of all filled electronic states for selected atom pairs were calculated by the Crystal Orbital Hamilton Population (COHP) method.

IV. Results and discussion

IV.A. Crystallographic structure

IV.A.1. X-Ray diffraction analysis. The X-ray diffraction pattern of the powdered SPS pellets of $Mg_3Sb_{2-x}Bi_x$ have been identified by X-ray diffraction and the spectra are shown in Fig. 2. On comparing with the JCPDS data; card no. 00-003-0375), a single phase β-Mg_3Sb_2 (hexagonal; space group $P\bar{3}m1$) with no detectable impurities of other phases was found. A detailed analysis of XRD patterns was carried out using Reitveld refinement and the cell parameters were calculated. Under ambient conditions, the lattice parameters, *a* and *c* for Mg_3Sb_2 was determined to be 4.57 Å and 7.24 Å, respectively. The best fit of the XRD data yielded the *z* coordinates for Mg(II) and Sb atoms as (1/3,2/3,0.634) and (1/3,2/3,0.228) to the 2d Wyckoff positions. For $Mg_3Sb_{2-x}Bi_x$ alloys the lattice parameter were extrapolated from Reitveld refinement and were found increasing with increasing Bi content, being consistent

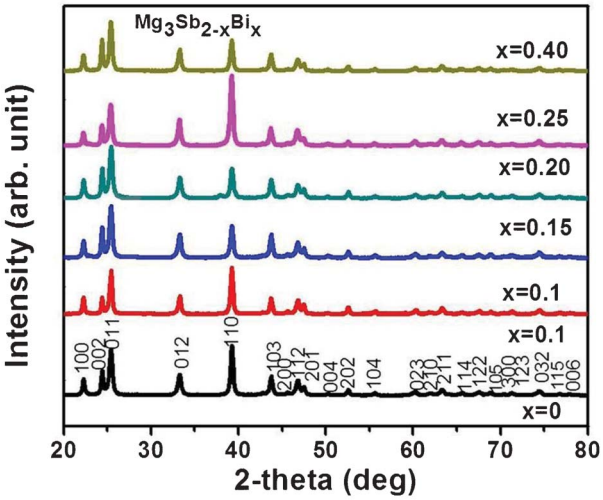

Fig. 2 (a) X-Ray diffraction pattern of $Mg_3Sb_{2-x}Bi_x$; $0 \leqslant x \leqslant 0.4$ showing the single phase of Mg_3Sb_2 and single solid solution phase in Bi doped Mg_3Sb_2. The (hkl) indices of the undoped sample are marked at the bottom of the figure ($x = 0$).

with the Vegard's law as shown in supplementary Fig. S1, ESI.† As Vegard's law is complied by all solid solution with atomic level random distribution, all samples are thus considered as solid solutions. The increase in the lattice parameters is consistent with the increasing ionic radii of Bi ions, while the broadening of the peaks is due to chemical disorder in the Sb sub-lattice of Mg_3Sb_2. The absence of any additional prominent peaks other than β-Mg_3Sb_2 structure in the XRD spectrum unambiguously confirms the solubility of Bi in the Sb sub-lattice.

IV.A.2. Scanning and transmission electron microscopy. In order to confirm the phase purity at microscopic and atomic scale, crystal structure, grain size distribution, homogeneities and densification in terms of closed packed grain boundaries of β-Mg_3Sb_2, SEM and TEM investigations were carried out. SEM investigation was carried out to observe the homogeneities of all samples and compositional analysis was done employing by SEM-EDAX. The homogeneities of samples were assessed by averaging the compositions of 8 different grains of each sample and taking the average as shown in Table 1 marked as SEM-EDAX compositions. All samples were found to be macroscopically homogeneous. The compositions of the consolidated ingots were also determined by XRF. Table 1 lists the XRF and SEM-EDAX determined compositions (marked as actual compositions) with surface compositions analyzed by photoemission spectroscopy measurement which shows a very close matching to nominal compositions. Bright field TEM images of SPS processed specimens of Mg_3Sb_2 and $Mg_3Sb_{1.8}Bi_{0.2}$ are shown in Fig. 3. Wide range of grain sizes (~5 to 120 nm) of β-Mg_3Sb_2 phase for both the specimens (Fig. 3a and 3c) was observed. The grains are densely packed and are uniform with respect to the composition. A selected area electron diffraction (SAED) pattern recorded from one of these grains, shown in the inset (Fig. 3a), was indexed as the β-Mg_3Sb_2 hexagonal structure along the $[01\bar{1}0]$ zone axis with

Table 1 Nominal and actual composition measured by different techniques, and carrier concentration, electrical conductivity and mobility at room temperature for $Mg_3Sb_{2-x}Bi_x$ alloys. XPS investigation was only carried out for Mg_3Sb_2 and $Mg_3Sb_{1.8}Bi_{0.2}$

Nominal compositions	Actual compositions (SEM-EDAX)	Actual compositions (XRF)	Actual compositions (XPS)	Carrier concentration n (10^{20} cm^{-3})	Electrical conductivity σ (S m^{-1})	Mobility μ (cm^2 V^{-s})
Mg_3Sb_2	$Mg_{59.5}Sb_{40.5}$	$Mg_{59.8}Sb_{40.2}$	$Mg_{60}Sb_{40}$	1.1	206.3	30
$Mg_3Sb_{1.9}Bi_{0.1}$	$Mg_{59.8}Sb_{38}Bi_{2.2}$	$Mg_{60.1}Sb_{37.8}Bi_{2.1}$		1.9	297.4	25
$Mg_3Sb_{1.85}Bi_{0.15}$	$Mg_{59.4}Sb_{37.6}Bi_{3.0}$	$Mg_{59.7}Sb_{37.4}Bi_{2.9}$		2.3	316.9	22.2
$Mg_3Sb_{1.8}Bi_{0.20}$	$Mg_{59.9}Sb_{36.5}Bi_{3.6}$	$Mg_{60.2}Sb_{36}Bi_{3.8}$	$Mg_{61.6}Sb_{36.9}Bi_{1.5}$	2.9	338.4	18.6
$Mg_3Sb_{1.75}Bi_{0.25}$	$Mg_{60.1}Sb_{36.5}Bi_{4.8}$	$Mg_{59.6}Sb_{35.5}Bi_{4.9}$		4.2	367.2	13.9
$Mg_3Sb_{1.6}Bi_{0.4}$	$Mg_{59.9}Sb_{36.5}Bi_{7.2}$	$Mg_{59.8}Sb_{32.4}Bi_{7.8}$		15	3460.4	36.9

lattice parameters a = 4.57 Å and c = 7.24 Å which are consistent with the XRD data.

The elemental composition of specimens estimated from energy spectroscopy analysis (EDAX) in our TEM was observed to be consistent with the nominal composition of Mg_3Sb_2. Several atomic scale images were recorded to understand the presence of different orientations of the crystallographic planes and their interface boundaries at atomic scale. Fig. 3b elucidates three such grains adjacent to each other sharing a triple junction (marked with arrows) with the presence of the planes $11\bar{2}0$ (0.231 nm), $10\bar{1}3$ (0.212 nm) and $11\bar{2}2$ (0.193 nm) of Mg_3Sb_2. The micrograph (Fig. 3b) clearly reveals that the individual grains are truly crystalline with stacking of different planes and with random orientation with respect to each other. A corresponding SAED taken from the collective grain shows a set of Debye rings (inset in Fig. 3b)

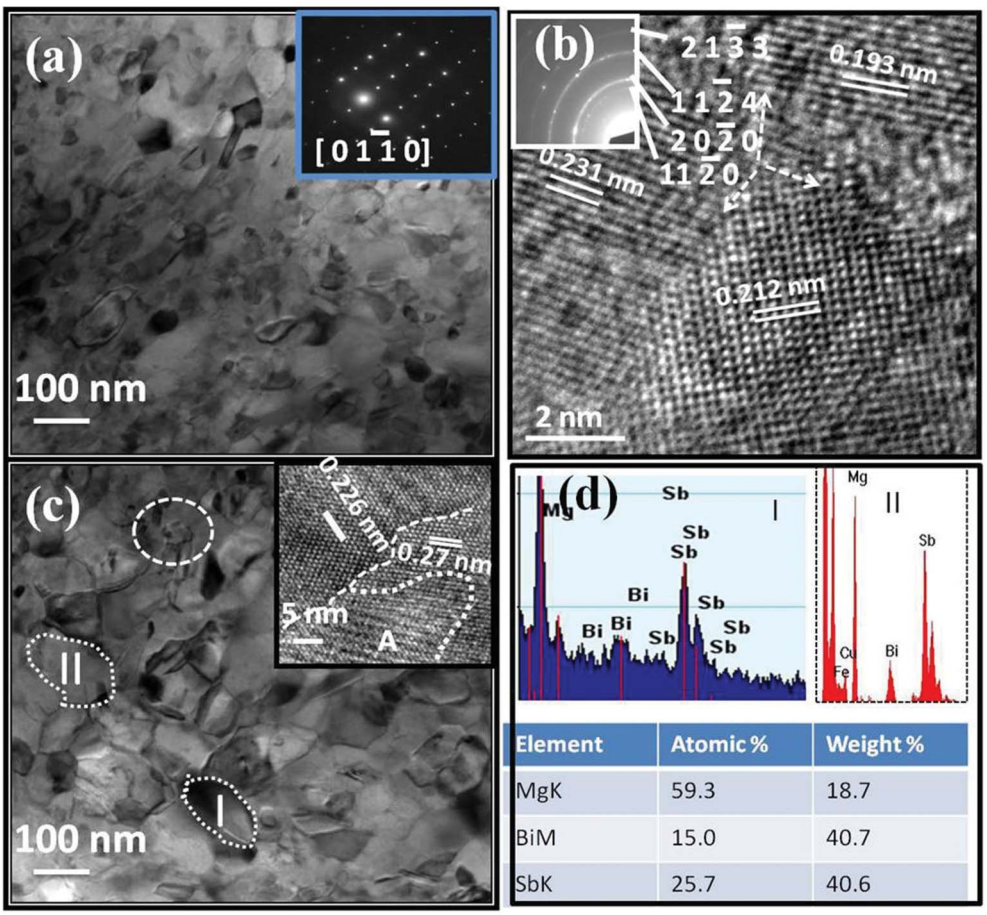

Fig. 3 a) Bright field electron micrograph recorded from the specimen of Mg_3Sb_2 showing highly densified grains and sharp grain boundaries. SAED in the inset clearly reveals of β-Mg_3Sb_2-type hexagonal structure, b) atomic scale images from the same specimen exhibits the presence of different orientations of the crystallographic planes and their interface boundaries. c) Bright field electron micrograph recorded from the specimen of $Mg_3Sb_{1.8}Bi_{0.2}$ shows densely packed grains. The atomic scale image in the inset exhibits high crystallinity of the material. d) EDS-TEM patterns recorded from the specimen of $Mg_3Sb_{1.8}Bi_{0.2}$ shows all the constituent elements; Mg, Sb and Bi throughout in the microstructure.

constituted of very fine set of sharp spots. The analysis of these rings reveals that the material exhibits a single phase Mg_3Sb_2 with lattice planes, h k l : $11\bar{2}0$, $20\bar{2}0$, $11\bar{2}4$, $21\bar{3}3$ having interplaner spacing of 0.229, 0.198, 0.142, 0.127 nm respectively, of hexagonal crystal structure, space group $P\bar{3}ml$. Fig. 3c shows bright field electron micrograph corresponding to the specimen of $Mg_3Sb_{1.8}Bi_{0.2}$ The grains were found to be again densely packed and were observed to be little larger than that of bare Mg_3Sb_2. In the first sight, it may seem that the small precipitates inside the grain marked by circle in Fig. 3c could arise from some impurity phase. However, atomic scale imaging of the microstructure from this region shown in the inset (Fig. 3c) reveals a clear contrast of well defined planes of $11\bar{2}0$ and $10\bar{1}2$ with the inter planar spacings of 0.226 and 0.27 nm, respectively, of Mg_3Sb_2 hexagonal crystal structure. A curly boundary has been highlighted by a dotted line at the interface separating the two grains (Inset Fig. 3c). The Moiré fringes evolved due to overlap of thin crystals are also observed in the micrograph (region 'A' as marked by dotted line in the inset Fig. 3c). EDAX-TEM patterns recorded at different regions marked as grain I and grain II (Fig. 3c) in the microstructure of $Mg_3Sb_{1.8}Bi_{0.2}$ shown in Fig. 4d clearly shows the presence of the elements; Mg, Sb and Bi, throughout the microstructure.

IV.B. Transport properties

IV.B.1. Electronic transport. Fig. 4 shows the temperature dependence of electrical conductivity σ (T), thermopower S (T) and power factor (σ^2 S (T)) of the $Mg_3Sb_{2-x}Bi_x$ samples. Regardless of the temperature, the σ (T) of the Bi doped samples is found to be larger than that of the undoped samples (Fig. 4a). The σ (T) increases monotonically with temperature for $x \leqslant 0.25$ alloys throughout the temperature range of 300 K to 750 K, displaying semiconducting behavior (Fig. 4a). However, for $Mg_3Sb_{1.6}Bi_{0.4}$ alloys σ (T) decreases with rising temperature up to $\sim$610 K showing semiconductor–metallic transition with increasing x. The saturation in σ (T) above 610 K infers to a semi-metallic characteristics for higher Bi concentration in $Mg_3Sb_{2-x}Bi_x$. The positive values of S (T) data as shown in Fig. 4b indicates that all alloys are p-type semiconductors. On the other hand, S (T) increases with temperature up to certain maximum in the range of 600–700 K. The magnitude of S_{max} (T) also steadily increases from 327 $\mu V\ K^{-1}$ in Mg_3Sb_2 to 410 $\mu V\ K^{-1}$ for $x = 0.15$ at the temperature 650 K. With further increase in the Bi concentration, S_{max} (T) decreases and is 275 $\mu V\ K^{-1}$ for $x = 0.40$, which is lower than the undoped system. Fig. 4c shows the temperature dependent behavior of power factor. We find that for small Bi concentration, the low temperature variation in the power factor is governed largely by S (T), however for higher temperatures, it is governed by σ (T). The maximum power factor was realized in $Mg_3Sb_{1.8}Bi_{0.2}$ which was around 41.8 $\mu W\ cm^{-1}\ K^{-2}$ which is comparable with that of the Bi_2Te_3-based thermoelectric materials.[78,79]

Comparison of our data of Mg_3Sb_2 with that of the earlier reports by Kajikawa *et al.*[64] and Condron *et al.*[65] shows similar trends in the variation of σ (T) and S (T), however with the difference in the magnitudes. For example, our S_{max} (T) of 327 $\mu V\ K^{-1}$ at 660 K falls less than the values reported by Kajikawa

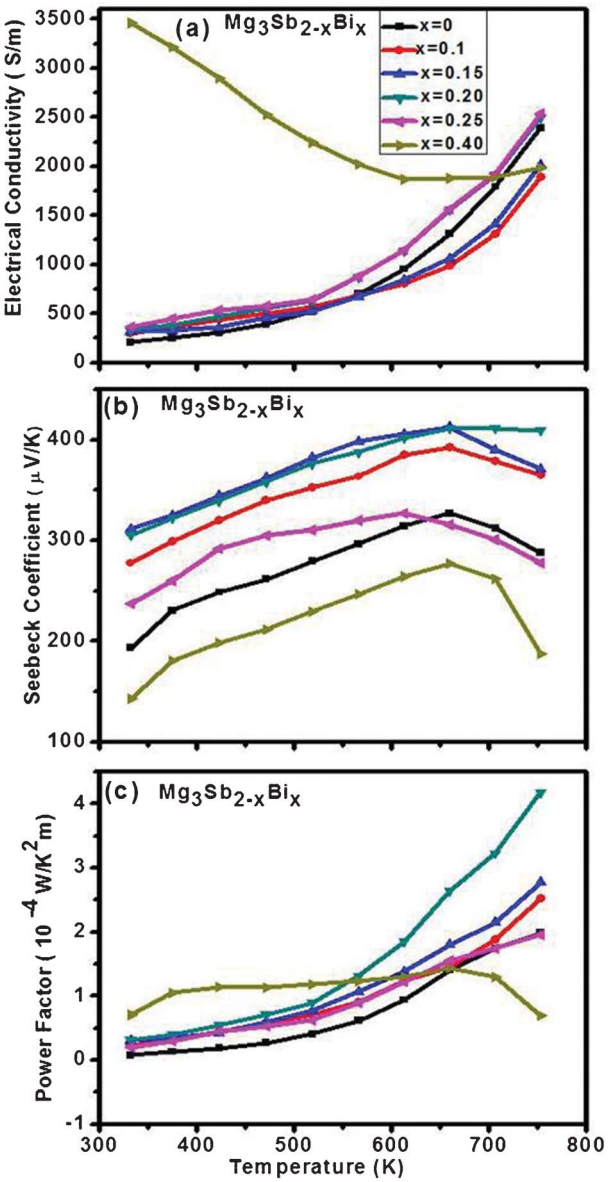

Fig. 4 Temperature dependence of the electronic transport properties of $Mg_3Sb_{2-x}Bi_x$ ($0 \leqslant x \leqslant 0.4$). (a) Electrical conductivity σ (T); Seebeck coefficient S (T); (c) power factor, (σ^2S (T)).

et al.[64] ($S_{max}(T)$ = 550 $\mu V\ K^{-1}$) and Condron *et al.*[65] (S_{max} (T) = 445 $\mu V\ K^{-1}$).

Similarly, σ (T) of our sample is 2395 S m^{-1} at 750 K which is lower than all three samples reported by Kajikawa *et al.*[64] and higher than that reported by Condron *et al.*[65] The differences in σ (T) and S (T) may be associated with the sample synthesis process and sample quality. We note that in the present sample synthesis, sintering were carried out at 1073 K which is much lower than any of the samples prepared by Kajikawa *et al.*[64] Considering the volatility and oxidation of Mg, sintering at a lower temperature helps in achieving better stoichiometry and also free from oxidation giving rise to a higher σ (T). Moreover, it is noteworthy that in all earlier reports, mixed phases such as Mg_3Sb_2, MgO and Sb

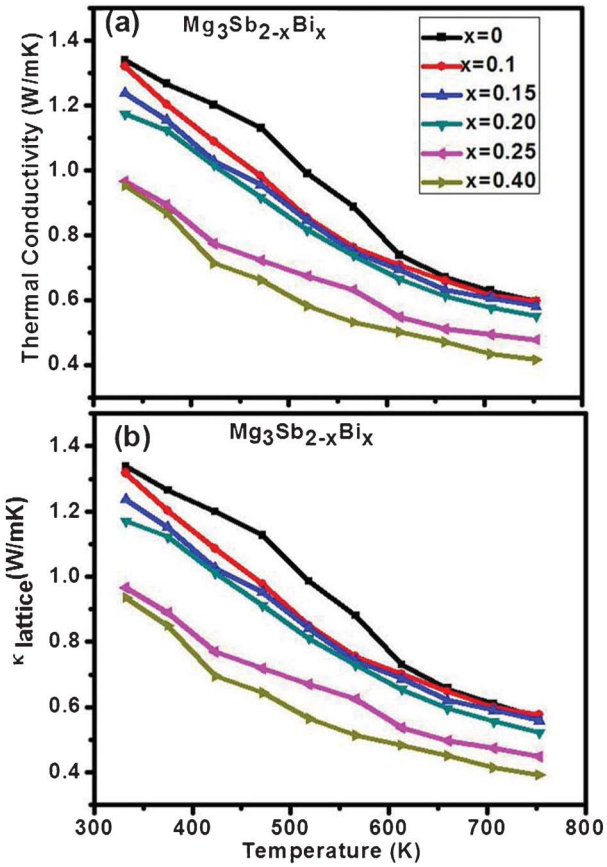

Fig. 5 Temperature dependence of the thermal transport of $Mg_3Sb_{2-x}Bi_x$ ($0 \leqslant x \leqslant 0.4$), (a) total thermal conductivity κ (T), (b) lattice thermal conductivity $\kappa_{lattice}(T)$.

precipitates were observed which were attributed to heterogeneous mixture. However, in the present studies, all the sample of $Mg_3Sb_{2-x}Bi_x$ ($0 \leqslant x \leqslant 0.4$) were of single phase with elemental stoichiometries nearly same as the nominal composition (Table 1).

IV.B.2. Thermal transport. Fig. 5 shows the temperature dependence of thermal conductivity κ (T) of $Mg_3Sb_{2-x}Bi_x$ alloys. Interestingly, the total thermal conductivity decreases with increasing Bi concentration in Mg_3Sb_2 alloy regardless to the temperature as shown in Fig. 5a. The temperature dependent of κ decreases with temperature displaying $1/T$ type behavior commonly occurred in the bulk crystalline solids. Interestingly, the thermal conductivity observed in the present alloys is significantly small compared to that of Bi_2Te_3 based alloys.[78,79] Wiedemann–Franz law has been used to calculate the lattice thermal conductivity ($\kappa_{lattice}$) by subtracting electronic thermal conductivity ($\kappa_e = L\ \sigma\ T$, where L is Lorentz number, σ, the electrical conductivity and T, the temperature in K) from the total thermal conductivity. Here, we use the temperature dependent Lorentz number[80] and the bipolar contribution was taken into account by assuming $\kappa_{lattice} \sim 1/T$.[81] Fig. 5b represents the temperature dependent lattice part of thermal conductivity. The lattice part of thermal conductivity in all the samples of $Mg_3Sb_{2-x}Bi_x$ ($0 \leqslant x \leqslant 0.4$)

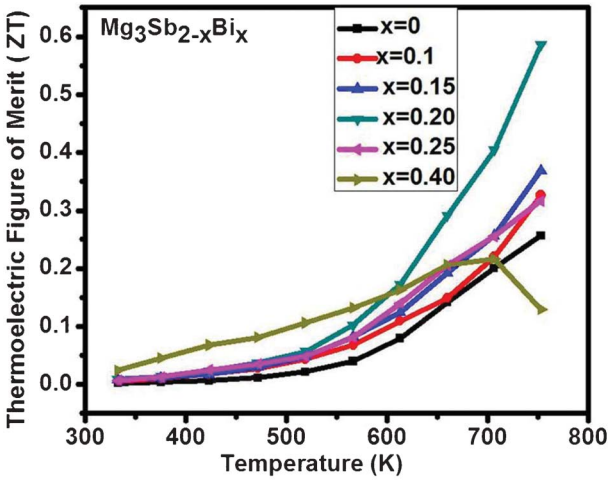

Fig. 6 Temperature dependence of thermoelectric figure of merit of $Mg_3Sb_{2-x}Bi_x$ ($0 \leqslant x \leqslant 0.4$).

alloys was observed to decrease with increasing temperature. One could not find significant differences (Fig. 5a and 5b) in total and lattice thermal conductivity because the electronic part of thermal conductivity is negligibly small due to very low value of electrical conductivity.

The temperature dependence of ZT of $Mg_3Sb_{2-x}Bi_x$ alloys is displayed in Fig. 6. The maximum ZT for Mg_3Sb_2 was observed to be about 0.26 at temperature of 750 K which is significantly higher $ZT \approx 0.21$ at 875 K reported by Condron *et al.*[65] Interestingly, the optimum doping of Bi with 0.2 at% in Mg_3Sb_2 alloy, remaining semiconducting in nature, drives the system to an increased $ZT \approx 0.60$ at 750 K. This enhancement in ZT is about 130% larger than the ZT value observed in parent Mg_3Sb_2 compound. The enhanced ZT is resulted from the increase in power factor with simultaneous decrease in total thermal conductivity.

IV.C. Electronic structure

IV.C.1. X-Ray photo emission spectroscopy. *X-Ray photo electron spectroscopy.* Fig. 7a and 7b show the Mg 1s and Sb 3d core levels of Mg_3Sb_2, $Mg_3Sb_{1.8}Bi_{0.2}$ and pure Mg metal. Mg 1s and Sb 3d core levels of pure metals have been shown as the bottom spectrum of Fig. 7a and 7b respectively. For pure Mg, small oxide feature centered around 2.0 eV above the main peak is also visible. First bulk ($1w_p$) and surface ($1w_s$) plasmons are clearly observed in Mg 1s core level of elemental Mg. However, these are quite weak for undoped and doped Mg_3Sb_2 due to semiconducting nature of these alloys. Small oxide feature centered around 3.4 eV above main peak has also been observed for Sb $3d_{5/2}$ and $3d_{3/2}$ peaks. Evolution of core levels with progressive mechanical scrapping and related oxide features are discussed in more detail in the supporting information (Fig. S2, ESI† and related text). No significant changes in the binding energy (BE) positions and lineshape of core levels between the undoped and the doped samples were detected, suggesting a little alterations of the local chemical environment. For undoped and doped Mg_3Sb_2, Mg 1s is located at 1305.0 eV BE, while the Sb $3d_{5/2}$ and $3d_{3/2}$ are

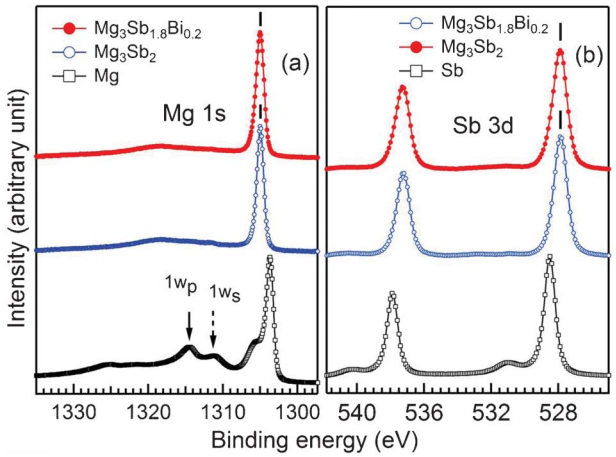

Fig. 7 Comparison of (a) Mg 1s and (b) Sb 3d core level spectra of Mg_3Sb_2 (open circle), $Mg_3Sb_{1.8}Bi_{0.2}$ (filled circle) and pure Mg and Sb metals (squares). Peak positions are indicated by ticks. For Mg 1s, bulk (w_p) and surface (w_s) plasmons are indicated by solid and dashed arrows respectively. All the spectra have been normalized to the same peak height for comparison. Spectra have been vertically staggered for clarity of presentation.

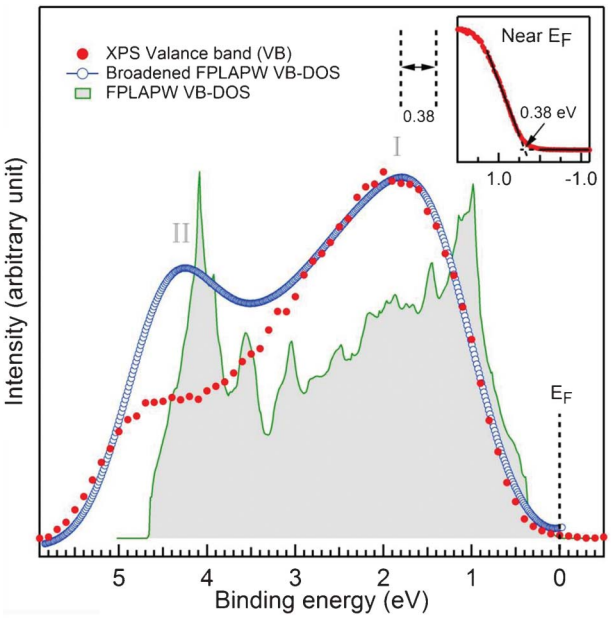

Fig. 8 Shirley-background subtracted valence band XPS spectrum of Mg_3Sb_2 (filled circles) and calculated VB density of states (DOS) using FPLAPW code shown without (shaded) and with 0.4 eV Gaussian broadening (open circles). Broadened VB DOS is horizontally shifted by 0.38 eV for comparison with the XPS VB. All the spectra have been normalized to the same peak height. Position of Fermi level is indicated by a dashed line. Inset shows the close up of XPS VB near Fermi level. Linear fits applied to determine valence band maximum are also shown in the inset.

located at 527.9 and 537.3 eV BE, respectively, with spin orbit splitting of 9.4 eV. However, in comparison to the pure elemental metal (1303.7 and 528.5 eV BE for Mg 1s and Sb 3d5/2, respectively), we find significant shift in the BE positions of both Mg 1s and Sb 3d in Mg_3Sb_2 which is clearly indicated by ticks. Thus, for the undoped and doped Mg_3Sb_2 compounds, the Mg 1s is shifted towards higher binding side by 1.3 eV with respect to elemental Mg and Sb 3d is shifted towards lower binding energy side by 0.6 eV with respect to the elemental Sb.

It is interesting to note that BE shifts in Mg 1s and Sb 3d are in opposite directions. Differences in the electronegativity of Mg (1.31) and Sb (2.05)[82] suggest the charge transfer from Mg to Sb in Mg_3Sb_2. Such charge transfer results in shift of Mg (Sb) core levels towards higher (lower) BE side compared to pure metals indicating the chemical bonding between these atoms to be ionic in nature. This charge transfer picture is also supported by our theoretical calculations (Fig. 11 and related discussion).

The XPS valence band (VB) spectrum of Mg_3Sb_2 is shown in Fig. 8 along with the theoretically calculated density of states (DOS). As evident, the XPS VB mainly comprises of two peaks: one centered around 1.8 eV BE and the other centered around 4.4 eV BE. In order to determine the valence band maximum (VBM), we adopt to the method based on linear fits which has been successfully employed for a variety of materials.[83] Intersection of two straight lines, *i.e.*, a fit to leading edge of VB and the other to the background between VBM and the Fermi energy (E_F) provides a reasonable measure of the VBM.

We have located VBM to be 0.38 eV below E_F from the extrapolation of linear fits as shown in the inset of Fig. 8. We find that there is an excellent agreement between experimental and theoretical VB DOS, when the latter is shifted by 0.38 eV to match the experimental VBM. We note that the E_F in theoretical calculations is a reference level scaled to zero on the energy scale, and thus it is legitimate to shift the DOS spectrum for comparison with the experimental data. The energy position of peaks I and II and XPS VB leading edge are reproduced in the theoretical VB DOS, however with a disagreement in the intensity of peak II (Fig. 9). This may be attributed to the difference in sub-shell photoemission cross

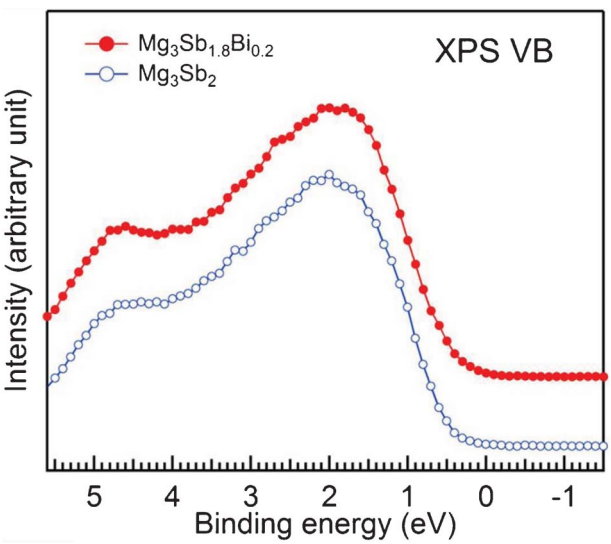

Fig. 9 XPS valence band of Mg_3Sb_2 (open circle) and $Mg_3Sb_{1.8}Bi_{0.2}$ (filled circle). Spectra have been normalized to have the same height at their peak.

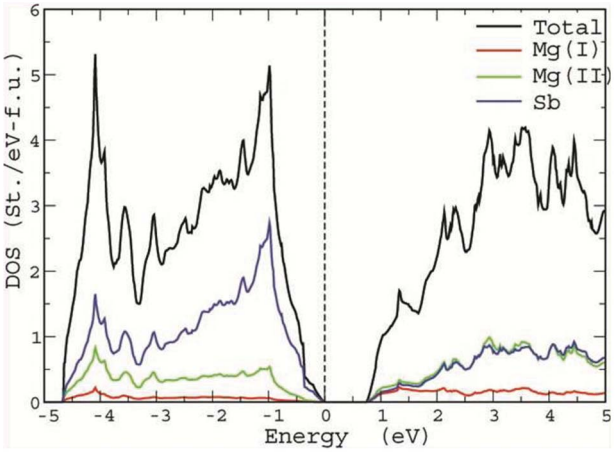

Fig. 10 The mBJ-GGA calculated total and atom-resolved density of states of Mg_3Sb_2. The dashed line through energy zero represents the Fermi level.

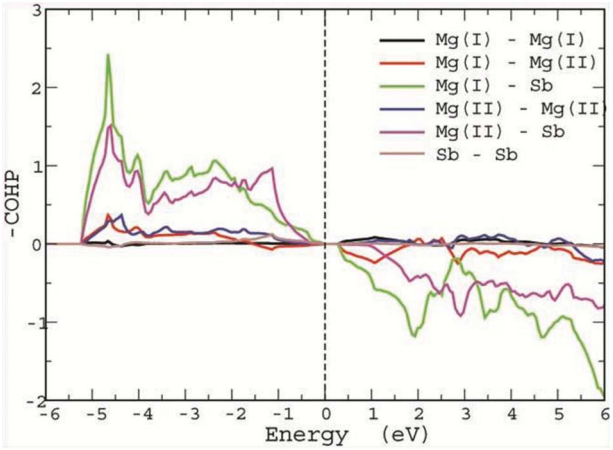

Fig. 11 The LMTO-ASA generated COHP analysis of various bonds (as given in the legends) of Mg_3Sb_2. The dashed line through energy zero represents the Fermi level. The zero of –COHP axis differentiates bonding (positive values of –COHP) and antibonding (negative values) states.

sections which are not included in the DFT calculations. Origin of peaks I and II can be realized by comparing the contributions of partial DOS of Mg and Sb to the total calculated DOS. On comparison of Fig. 8 and 10, we identify that the peak I and II are related to hybridized Sb 5p and Mg 3s states with dominant Sb 5p character. An earlier XPS report of Mg_3Sb_2 failed to provide a clear resolution of these two peaks.[80] The consistency between the experimental and theoretical DOS spectrum therefore reflects the high quality of our samples and the preparation of clean surface.

Fig. 10 shows the comparison of XPS valence band of Mg_3Sb_2 and $Mg_3Sb_{1.8}Bi_{0.2}$. Due to small impurity concentration and being isoelectronic, no significant change in the shape or energy positions could be detected between the undoped and Bi doped samples. This is also supported by the fact that no significant change in the BE position and line shapes of core levels of undoped and Bi doped samples were found as shown in Fig. 7.

IV.C.2. First-principles calculations. *Density of states (DOS).* To describe the density of states, chemical bonding and band structure we have performed calculations using both FP-LAPW and the LMTO-ASA methods. Results of the LMTO-ASA calculations have been utilized mainly for the interpretation of bonding through COHP analyses, which renders a deeper insight into the nature of the cooperative bonding in the solid. The FP-LAPW method, which is more accurate, because of its shape free approximation to the muffin-tin potential, has been used to interpret the fat-band analyses of the band structure and atom/orbital resolved contribution to the total density of states.

From the above discussions, it is evident that the DFT generated density of states with mBJ exchange correlation functional provides a good agreement with the XPS spectra. Although we find that the overall features of the DOS spectra are similar in the local density approximation (LDA) and in generalized gradient approximations (GGA), mBJ functional yielded a band gap of 0.7 eV, (Fig. 10) in comparison to 0.1 and 0.2 eV obtained by LDA and GGA, respectively, consistent with the previous reports.[84,85]

Detailed analysis of the mBJ DOS reveal that the valence bands are spread to about 10 eV and can be broadly divided into two main parts. The first part is the low lying band located at about 9 eV (not shown in Fig. 10) which mainly comprise the Sb 5s states and thus are chemically inactive. The second part is located from -5 eV to EF and are dominated by the Sb 5p with little admixture of the Mg 3s states. The lower conduction band is primarily composed of the Mg 3s states. We also note that the overall features of the DOS structure are similar in both FP-LAPW and LMTO-ASA method, except for the magnitude of the energy band gap. In LMTO-ASA method, the gap magnitude is estimated to be ≈ 0.2 eV, when exchange correlations were treated in the GGA formalism.

Chemical bonding. To analyze the nature of chemical bonding properties, we perform COHP analyses as implemented in the LMTO-ASA suite of programs. The COHP gives the energy contributions of all electronic states for a selected bond. Since the values are negative (positive) for bonding (antibonding) states, we plot the –COHP spectrum to get positive values according to the well-known –COHP diagrams. The calculated –COHP plots for selected interactions, cumulated over all bonds per unit cell, are shown in Fig. 11.

Following the crystal structure details, the inequivalence of two Mg sites infers to two different bonding characteristics between the Mg(I)–Sb and Mg(II)–Sb bonds. Fig. 11 shows the –COHP curves of the Mg(I), Mg(II), and Sb pairs in Mg_3Sb_2. The Mg(I)–Sb and Mg(II)–Sb bonding states dominate the occupied part of the –COHP spectrum, however differ in their bond strengths. Also it may be noted that character of electronic states in the vicinity of E_F is strongly dominated by the Mg–Sb bonding states. The Integrated –COHP bonding energy of the Mg(II)–Sb bond in the $(Mg_2Sb_2)^{2-}$ motif is ~ 3.5 times larger than the Mg(I)–Sb bond (0.5 eV). One also observes that there is small, yet finite, bonding features between the Mg(I)–Mg(II) and Mg(II)–Mg(II) pairs, which are higher in strength compared to the Sb–Sb bonding, which however can be partly

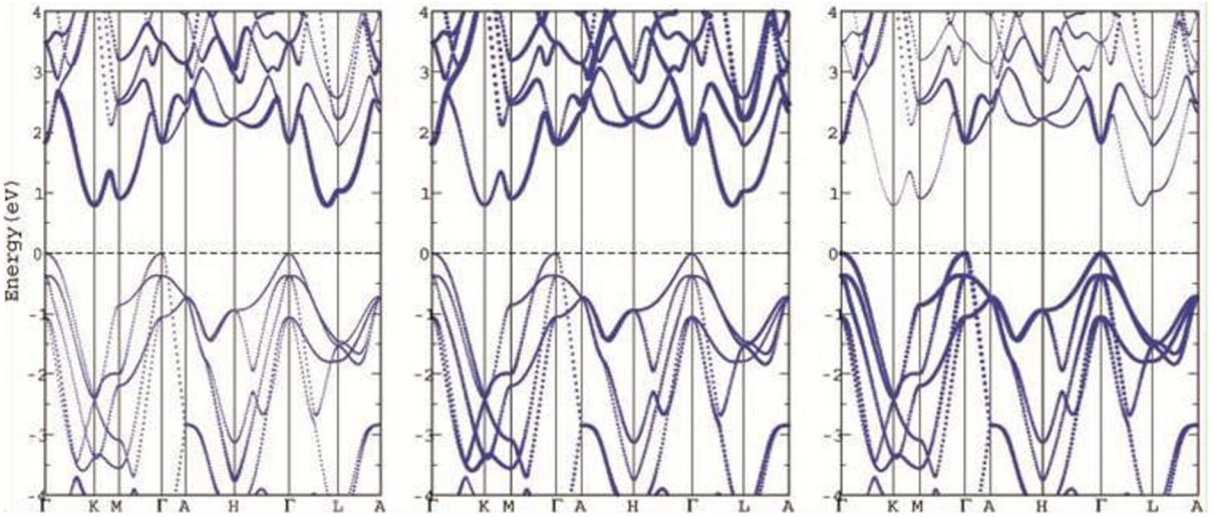

Fig. 12 The mBJ-GGA generated band structure of Mg_3Sb_2 as obtained from the FP-LAPW method. The left, middle and right panels are the fat-band representation of the Mg(I), Mg(II) and Sb states, respectively. The broken line through energy zero represents the Fermi level.

accounted in terms of their bond distances. Interestingly, we find few bonding states above E_F, characteristics of the Mg(I)–Mg(I) and Mg(II)–Mg(II) bond pairs. This suggests that charge transfer from the Mg to Sb orbitals is not fully complete in Mg_3Sb_2. We note that this is not a computational artifact emerging due to the atomic sphere radii, as we have cross examined the effect with different space filling geometries. Thus, from the perspectives of the materials chemical bonding, the electrochemical structure of bulk Mg_3Sb_2 may be expressed as $Mg(I)^{2+}$–$[Mg_2Sb_2]^{2-}$, showing that Mg(I) is relatively more ionic while the Mg(II)–Sb and Sb–Sb interactions in the solid are covalent in nature. The picture is more evident in the band structure analysis which is presented below.

Band structure. The band dispersion relations calculated for Mg_3Sb_2 along the highly symmetrical paths are presented in Fig. 12, where the Mg(I) (left panel), Mg(II) (middle panel) and Sb (right panel) contributions to the overall spectrum are indicated by the fat-band representation. While the valence band maximum peaks at the Γ-point (zone center), the conduction band minimum is determined to be at the K-point, which is also degenerate with the a point along the Γ-L segment of the hexagonal Brillouin zone. This indicates that Mg_3Sb_2 is an indirect band gap semiconductor. The top of the valence bands, which are dominated by the Sb 5s states, are significantly dispersed over wider energy range manifesting the covalent Sb–Sb bonding in Mg_3Sb_2, which is consistent with out –COHP analysis. It is also observed that the dispersion of the Sb 5s states along the Γ–A and Γ–M directions are very different indicating high anisotropy in the electronic conductivity in Mg_3Sb_2. The band dispersion along Γ–A is representative of the interactions between the atoms in the basal *a*–*b* plane of the hexagonal unit cell in real space, while the Γ–M manifests the interactions along the *c*-axis of the unit-cell.

It is also interesting to note the distribution of the Mg(I) and Mg(II) states, following the fat-band analyses. No significant 3s character of the Mg(I) atoms is determined in the valence band, suggesting a complete charge transfer and thus Mg(I) atoms render a ionic character in the system. However, the case for the Mg(II) atoms seems to be different. Analysis show small degree of Mg 3s character for the Mg(II) atoms in the valence band (see middle panel of Fig. 12), which is $\approx$1.5 eV along the AH direction of the BZ, and $\approx -2.4 < E(eV) < 3.6$ along the ΓKM segments. Due to their relatively higher binding energies, these Mg 3s states are expected to be less active in the materials transport properties. Interestingly, it is also found that some of the Sb 5p characters are distributed in the empty conduction band centered on the Γ′-point. With few Mg(II) 3s character being in the valence band and few Sb 5p states in the unoccupied region of the electronic structure, suggests that Mg_3Sb_2 is not a fully charge transferred semiconductor which is quite typical of the Zintl phase compounds. Thus representation of the materials chemical structure as $Mg(I)^{2+}[Mg_2(II)–Sb_2]^{2-}$ seems to be appropriate suggesting a fully ionic Mg(I) atom with a certain degree of covalency between the Mg(II)–Sb and Sb–Sb bonds. The Mg(II)–Sb bonding characteristics seems to be very crucial, since Mg vacancies would generate more hole states in the Sb p bands, thereby accounting for p-type carrier conduction in Mg_3Sb_2.

Beyond, the higher reactivity of Mg(II) atoms over Mg(I) atoms is also observed upon chemical substitutions in the Mg_3Sb_2. It is reported that the impurities, such as Zn, Sm and others,[85–87] when incorporated in Mg_3Sb_2 occupy the Mg(II) site and not the Mg(I) site, showing that the two Mg atoms occupying the two different crystallographic positions in Mg_3Sb_2 are very different from chemical perspectives.

According to Mott's equation,[88] the performance of a thermoelectric material depends on the density of states effective mass, or in other words heavy bands. However, such flat bands results in low mobility (μ). In the regime where the carriers are scattered by acoustic phonons the accepted

relation is $\mu \propto (m^*)^{-5/2}$. Thus, to optimize both effects, a combination of heavy and light bands would be crucial to optimize the electronic performance of a thermoelectric system. In Mg_3Sb_2, we observe such a scenario in its band structure. As discussed above, the top of the valence band is composed of heavy bands (along Γ–M) and light bands (Γ–A and H–Γ–L directions). Besides we also find similar characteristics about 0.4 below E_F where non-parabolic dispersion of bands are observed along various segments of the Brillouin zone, such as Γ–M, Γ–H and Γ–L. This partly accounts for the high power factor observed in p-type Mg_3Sb_2 materials.

With addition of Bi, which is isoelectronic with Sb, the overall features of the Mg_3Sb_2 band structure is expected to be preserved. However, due to the larger spatial extent of the Bi 6p orbitals, in comparison to the 5p orbitals of Sb, it is expected that the Sb–Bi band overlap would be relatively higher in comparison to the Sb–Sb bond overlaps. Thus, the bands along Γ–A and that along the H–Γ–L directions of the BZ are expected to more dispersed with respect to the undoped Mg_3Sb_2 system, thereby partly explaining the enhanced p-type conductivity in the Bi doped system. However, one also finds an increase in the cell parameters with Bi doping. As shown in the supporting Fig. S1, ESI,† the rate of increase in *c*-axis parameter is approximately twice larger than that of the '*a*' parameter, with Bi doping. Increase in cell volume usually leads to band narrowing effects. Such band narrowing effects would be more prominent along the Γ–M direction, since it represents the interaction along the *c*-axis. Thus, an increase in the *c*-parameter is expected to induce more non-parabolicity of the band along the Γ–M direction of the BZ, thereby enhancing the materials Seebeck coefficient. Thus, Bi doped Mg_3Sb_2 is a clear manifestation of a Zintl thermoelectric whose optimization of *ZT* is achieved due to the presence of both light and heavy bands, originating due to the anisotropy in chemical bonding.

V. Conclusions

Polycrystalline Zintl phase of Mg_3Sb_2 and its solid solution phase $Mg_3Sb_{2-x}Bi_x$ ($0 \leqslant x \leqslant 0.4$) were synthesized successfully employing spark plasma sintering technique in one step synthesis process, without any trace of oxides and Sb precipitates. A peak $ZT \approx 0.60$ at 750 K has been realized in $Mg_3Sb_{1.8}Bi_{0.2}$ alloy which is due to an increase in power factor with simultaneous decrease in thermal conductivity. For $x \geqslant 0.25$, we also observe that the system goes from a semiconducting to a metallic state. The electronic structure of Mg_3Sb_2 as revealed by X-ray photo-emission spectroscopy and DFT based calculations render consistent features of the valence band spectrum. The increase in the power-factor is associated with the presence of both light and heavy bands derived from the Sb states. Although, a significant improvement in *ZT* of the simple p-type $Mg_3Sb_{1.8}Bi_{0.2}$ alloy has been achieved in the present study, there remains appreciable scope for further improvement of its TE properties by suitable doping with heavy elements and also employing nanostructuring approaches. Besides, the synthesis of n-type Mg_3Sb_2 related alloys is equally important for device fabrication of the thermoelectric devices, which is currently under our investigation. Moreover, Mg_3Sb_2-based Zintl compounds being free from expensive rare earth elements makes these materials cost-effective, environmentally friendly, non-toxic, abundant and globally available, triggering thermoelectric research for the use of waste heat recovery.

Acknowledgements

This work was financially supported by CSIR-TAPSUN (CSIR-NWP-54) programme entitled ''Novel approaches for solar energy conversion under technologies and products for solar energy utilization through Networking''. One of the authors, AB, greatly acknowledges UGC-CSIR for financial support. We thank Dr. Avanish for generating the model for the crystal structure of β-Mg_3Sb_2 and Radheshyam and Naval K. Upadhyay are acknowledged for technical and experimental support. JJP thank Nitin Sharma and Trilok Bhardwaj for assistance with cluster computations at CSIR-NPL. SA would like to thank NPL for financial assistance.

References

1 G. A. Slack, in *CRC Handbook of Thermoelectrics*, ed. D. M. Rowe, CRC, New York, 1995, 407–440.
2 *Chemistry, Structure, and Bonding of Zintl Phases and Ions*, ed. S. M. Kauzlarich, VCH Publishers, Inc, New York, 1996.
3 D. M. Young and S. M. Kauzlarich, *Chem. Mater.*, 1995, **7**, 206–209.
4 F. Gascoin, S. Ottensmann, D. Stark, S. M. Haile and G. J. Snyder, *Adv. Funct. Mater.*, 2005, **15**, 1860–1864.
5 S. J. Kim and M. G. Kanatzidis, *Inorg. Chem.*, 2001, **40**, 3781–3785.
6 G. J. Snyder, M. Christensen, E. Nishibori, T. Cailat and B. B. Iversen, *Nat. Mater.*, 2004, **3**, 458–463.
7 S. Bhattacharya, R. P. Hermann, V. Keppens, T. M. Tritt and G. Snyder, *Phys. Rev. B: Condens. Matter Mater. Phys.*, 2006, **74**, 134108.
8 J. Nyl'en, M. Andersson, S. Lidin and U. Haussermann, *J. Am. Chem. Soc.*, 2004, **126**, 16306–16307.
9 S. M. Kauzlarich, *Inorg. Chem.*, 1990, **10**, 75.
10 T. Caillat, J. P. Fleurial and A. Borshchevsky, *J. Phys. Chem. Solids*, 1997, **58**, 1119.
11 D. T. Morelli and G. P. Meisner, *J. Appl. Phys.*, 1995, **77**, 3777.
12 B. C. Sales, D. Mandrus and R. K. Williams, *Science*, 1996, **272**, 1325.
13 G. S. Nolas, M. Kaeser, R. T. Littleton and T. M. Tritt, *Appl. Phys. Lett.*, 2000, **77**, 1855.
14 X. F. Tang, H. Li, Q. J. Zhang, M. Niino and T. Goto, *J. Appl. Phys.*, 2006, **100**, 123702.
15 X. Shi, H. Kong, C. P. Li, C. Uher, J. Yang, J. R. Salvador, H. Wang, L. Chen and W. Zhang, *Appl. Phys. Lett.*, 2008, **92**, 182101.
16 W. Y. Zhao, P. Wei, Q. J. Zhang, C. L. Dong, L. S. Liu and X. F. Tang, *J. Am. Chem. Soc.*, 2009, **131**, 3713.

17 G. S. Nolas, G. A. Slack and S. B. Schujman, in *Semiconductors and Semimetals*, ed. T. M. Tritt, Academic Press, San Diego, 2001, Vol. 69, 255.
18 G. S. Nolas, M. Beekman, J. Gryko, G. A. Lamberton, T. M. Tritt and P. F. McMillan, *Appl. Phys. Lett.*, 2003, **82**, 910.
19 M. Beekman and G. S. Nolas, *J. Mater. Chem.*, 2008, **18**, 842.
20 G. S. Nolas, J. L. Cohn, G. A. Slack and S. B. Schujman, *Appl. Phys. Lett.*, 1998, **73**, 178.
21 V. L. Kuznetsov, L. A. Kuznetsova, A. E. Kaliazin and D. M. Rowe, *J. Appl. Phys.*, 2000, **87**, 7871.
22 A. Saramat, G. Svensson, A. E. C. Palmqvist, C. Stiewe, E. Mueller, D. Platzek, S. G. K. Williams, D. M. Rowe, J. D. Bryan and G. D. Stucky, *J. Appl. Phys.*, 2006, **99**, 023708.
23 M. Christensen, G. J. Snyder and B. B. Iversen, in *Proc. 25th Inter. Conf*, Themoelectrics, 2006, 40.
24 J. H. Kim, N. L. Okamoto, K. Kishida, K. Tanaka and H. Inui, *Acta Mater.*, 2006, **54**, 2057.
25 G. K. H. Madsen, K. Schwarz, P. Blaha and D. Singh, *Phys. Rev. B: Condens. Matter*, 2003, **68**, 125212.
26 P. F. P. Poudeu, A. Gueguen, C. I. Wu, T. Hogan and M. G. Kanatzidis, *Chem. Mater.*, 2010, **22**, 1046–1053.
27 A. Zevalkink, E. S. Toberer, W. G. Zeier, E. F. Larsen and G. Snyder, *Energy Environ. Sci.*, 2011, **4**, 510–518.
28 X. Shi, J. Yang, J. R. Salvador, M. Chi, J. Y. Cho, H. Wang, S. Bai, J. Yang, W. Zhang and L. Chen, *J. Am. Chem. Soc.*, 2011, **133**, 7837–7846.
29 J. P. Sootsman, J. He, V. P. Dravid, S. Ballikaya, D. Vermeulen, C. Uher and M. G. Kanatzidis, *Chem. Mater.*, 2010, **22**, 869–875.
30 D. Y. Chung, K. S. Choi, L. Iordanidis, J. L. Schindler, P. W. Brazis, C. R. Kannewurf, B. Chen, S. Hu, C. Uher and M. G. Kanatzidis, *Chem. Mater.*, 1997, **9**, 3060–3071.
31 S. R. Brown, S. M. Kauzlarich, F. Gascoin and G. Snyder, *Chem. Mater.*, 2006, **18**, 1873–1877.
32 A. D. LaLonde, Y. Pei and G. Snyder, *Energy Environ. Sci.*, 2011, **4**, 2090–2096.
33 W. M. Yim and F. D. Rosi, *Solid-State Electron.*, 1972, **15**, 1121–1140.
34 R. Nesper, *Prog. Solid State Chem.*, 1990, **20**, 1.
35 C. Lupu, C. Downie, A. M. Guloy, T. A. Albright and J. G. Mao, *J. Am. Chem. Soc.*, 2004, **126**, 4386–4397.
36 X. Shi, Y. Pei, G. J. Snyder and L. Chen, *Energy Environ. Sci.*, 2011, **4**, 4086–4095.
37 J. Li, J. Sui, Y. Pei, C. Barreteau, D. Berardan, N. Dragoe, W. Cai, J. He and L. D. Zhao, *Energy Environ. Sci.*, 2012, **5**, 8543–8547.
38 A. Zevalkink, W. G. Zeier, G. Pomrehn, E. Schechtel, W. Tremel and G. Snyder, *Energy Environ. Sci.*, 2012, **5**, 9121–9128.
39 X. Shi, H. Kong, C. P. Li, C. Uher, J. Yang, J. R. Salvador, H. Wang, L. Chen and W. Zhang, *Appl. Phys. Lett.*, 2008, **92**, 182101.
40 J. P. A. Makongo, D. K. Misra, X. Zhou, A. Pant, M. R. Shabetai, X. Su, C. Uher, K. L. Stokes and P. F. P. Poudeu, *J. Am. Chem. Soc.*, 2011, **133**, 18843.
41 P. Sahoo, D. K. Misra, J. Salvador, J. P. A. Makongo, G. S. Chaubey, N. J. Takas, J. B. Wiley and P. F. P. Poudeu, *J. Solid State Chem.*, 2012, **190**, 29–35.
42 A. Bhardwaj, D. K. Misra, J. J. Pulikkotil, S. Auluck, A. Dhar and R. C. Budhani, *Appl. Phys. Lett.*, 2012, **101**, 133103.
43 G. S. Chaubey, Y. Yao, J. P. A. Makongo, P. Sahoo, D. K. Misra, P. F. P. Poudeua and J. B. Wiley, *RSC Adv.*, 2012, **2**, 9207–9213.
44 S. Sumithra, N. J. Takas, D. K. Misra, W. M. Nolting, P. F. P. Poudeu and K. L. Stokes, *Adv. Energy Mater.*, 2011, **1**, 1141–1147.
45 D. K. Misra, J. P. A. Makongo, M. R. Shabetai, P. Paudel, K. L. Stokes and P. F. P. Poudeu, *Sci. Adv. Mater.*, 2011, **3**, 1–8.
46 J. P. A. Makongo, D. K. Misra, J. R. Salvador, N. J. Takas, G. Wang, M. R. Shabetai, A. Pant, P. Paudel, C. Uher, K. L. Stokes and P. F. P. Poudeu, *J. Solid State Chem.*, 2011, **184**, 2948–2960.
47 S. Sumithra, D. K. Misra, C. Wei, H. Gabrisch, P. F. P. Poudeu and K. L. Stokes, *Mater. Sci. Eng., B*, 2011, **176**, 246–251.
48 N. J. Takas, P. Sahoo, D. K. Misra, H. Zhao, N. L. Henderson, K. Stokes and P. F. P. Poudeu, *J. Electron. Mater.*, 2011, **40**, 662–669.
49 G. Chen, M. S. Dresselhaus, G. Dresselhaus, J.-P. Fleurial and T. Caillat, *Int. Mater. Rev.*, 2003, **48**, 45–66.
50 G. Chen and A. Shakouri, *J. Heat Transfer*, 2002, **124**, 242–252.
51 Y. Lan, B. Poudel, Y. Ma, D. Wang, M. S. Dresselhaus, G. Chen and Z. Ren, *Nano Lett.*, 2009, **9**, 1419–1422.
52 B. Poudel, Q. Hao, Y. Ma, Y. Lan, A. Minnich, B. Yu, X. Yan, D. Wang, A. Muto, D. Vashaee, X. Chen, J. Liu, M. S. Dresselhaus, G. Chen and Z. Ren, *Science*, 2008, **320**, 634–638.
53 J. Zhang, S. Kutlu, G. Liu and N. Tansu, *J. Appl. Phys.*, 2011, **110**, 043710.
54 J. Zhang, H. Tong, G. Liu, J. A. G. S. Herbsommer, G. S. Huang and N. Tansu, *J. Appl. Phys.*, 2011, **109**, 053706.
55 H. Tong, J. Zhang, G. Liu, J. A. G. S. Herbsommer, G. S. Huang and N. Tansu, *Appl. Phys. Lett.*, 2010, **97**, 112105.
56 A. Sztein, H. Ohta, J. E. Bowers, S. P. DenBaars and S. Nakamura, *J. Appl. Phys.*, 2011, **110**, 123709.
57 B. N. Pantha, I. Feng, K. Aryal, J. Li, J. Y. Lin and H. X. Jiang, *Appl. Phys. Express*, 2011, **4**, 051001.
58 S. K. Bux, R. G. Blair, P. K. Gogna, H. Lee, G. Chen, M. S. Dresselhaus, R. B. Kaner and J. P. Fleurial, *Adv. Funct. Mater.*, 2009, **19**, 2445–2452.
59 C. Hin, M. S. Dresselhaus and G. Chen, *Appl. Phys. Lett.*, 2010, **97**, 251909.
60 E. Zintl and E. Z. Husemann, *Phys. Chem.*, 1933, **21B**, 138.
61 M. M. Ripoll, A. Haase and G. Brauer, *Acta Crystallogr., Sect. B: Struct. Crystallogr. Cryst. Chem.*, 1974, **30**, 2006.
62 J. H. Bredt and L. F. Kendall, *Proceedings-IEEE/AIAA*, 1966.
63 D. M. Verbrugge and J. B. J. Van Zytveld, *Non-Cryst. Solids*, 1993, **736**, 156–158.
64 T. Kajikawa, N. Kimura and T. Yokoyama, in: *Proceedings of the 22nd International Conference on Thermoelectrics*, 2003, 305.
65 C. L. Condron, S. M. Kauzlarich, F. Gascoin and G. J. Snyder, *J. Solid State Chem.*, 2006, **179**, 2252–2257.
66 J. J. Pulikkotil, H. N. Alshareef and U. Schwingenschlogl, *Chem. Phys. Lett.*, 2011, **514**, 54.
67 N. Singh and U. Schwingenschlögl, *Chem. Phys. Lett.*, 2011, **508**, 29–32.
68 X. J. Wang, M. B. Tang, H. H. Chen, X. X. Yang, J. T. Zhao, U. Burkhardt and Y. Grin, *Appl. Phys. Lett.*, 2009, **94**, 092106.

69 S. M. Park, S. J. Kim and M. G. Kanatzidis, *J. Solid State Chem.*, 2003, **175**, 310–315.
70 H. B. Ozisik, K. Colakoglu, G. Surucu and H. Ozisik, *Comput. Mater. Sci.*, 2011, **50**, 1070–1076.
71 L. Zhang, M. H. Du and D. Singh, *Phys. Rev. B: Condens. Matter Mater. Phys.*, 2010, **81**, 075117.
72 A. F. May, M. A. McGuire and D. Singh, *Phys. Rev. B: Condens. Matter Mater. Phys.*, 2012, **85**, 035202.
73 C. Coban, K. Colakoglu and Y. O. Ciftci, *J. Phys. Chem. Solids*, 2012, **73**, 917–924.
74 P. Blaha, K. Schwarz, G. K. H. Madsen, D. Kvasnicka and J. Luitz, *WIEN2k- An Augmented Plane Wave + Local Orbitals Program for Calculating Crystal Properties*, TU Wien, Vienna, Austria, 2001.
75 K. Schwarz and P. Blaha, *Comput. Mater. Sci.*, 2003, **28**, 259.
76 R. Tank, O. Jepsen, A. Burkhardt and O. K. Andersen, TB-LMTO-ASA Program, Version 4.7, Max-Planck-Institut fur Festkorperforschung, Stuttgart, Germany, 1995.
77 O. Jepsen and O. K. Z. Andersen, *Z. Phys. B: Condens. Matter*, 1995, **97**, 35.
78 X. Yan, B. Poudel, Y. Ma, W. S. Liu, G. Joshi, H. Wang, Y. Lan, D. Wang, G. G. Chen and Z. F. Ren, *Nano Lett.*, 2010, **10**, 3373–3378.
79 S. Sumithra, N. J. Takas, D. K. Misra, W. M. Nolting, P. F. P. Poudeu and K. L. Stokes, *Adv. Energy Mater.*, 2011, **1**, 1141–1147.
80 S. A. Chambers, T. Droubay, T. C. Kasper and M. Gutowski, *J. Vac. Sci. Technol., B*, 2004, **22**, 2205.
81 L. M. Watson, C. A. W. Marshall and C. P. Cardoso, *J. Phys. F: Met. Phys.*, 1984, **14**, 113.
82 W. S. Liu, B. P. Zhang, J. F. Li, H. L. Zhang and L. D. Zhao, *J. Appl. Phys.*, 2007, **102**, 103717.
83 H. Kitagawa, M. Wakatsuki, H. Nagaoka, N. H. Isoda, Y. Hasezaki and K. Y. Noda, *J. Phys. Chem. Solids*, 2005, **66**, 1635.
84 Y. Imai and A. Watanabe, *J. Mater. Sci.*, 2006, **41**, 2435–2441.
85 F. Ahmadpour, T. Kolodiazhnyi and Y. Mozharivskyj, *J. Solid State Chem.*, 2007, **180**, 2420–2428.
86 S. Gupta, A. K. Ganguli and J. D. Corbett, *Inorg. Chem.*, 2006, **45**, 8175–8178.
87 S. Q. Xia, P. King and S. Bobev, *Acta Crystallogr., Sect. E: Struct. Rep. Online*, 2006, **62**, i184–i186.
88 N. F. Mott and H. Jones, *The Theory of the Properties of Metals and Alloys*, Dover Publication, New York, 1958.

